magnetochemistry

MDPI

Communication

Slow Magnetic Relaxation in Neutral *0D* and *1D* Assemblies of a Mn(III) Schiff Base Complex and Heptacyanorhenate(IV)

Taisiya S. Sukhikh [1], Wernsdorfer Wolfgang [2] and Kira E. Vostrikova [1,*]

[1] Nikolaev Institute of Inorganic Chemistry SB RAS, 3 Lavrentiev Avenue, 630090 Novosibirsk, Russia
[2] Physikalisches Institut, Karlsruhe Institute of Technology, 1 Wolfgang-Gaede-Str., D-76131 Karlsruhe, Germany
* Correspondence: vosk@niic.nsc.ru

Abstract: The first neutral *0D* and *1D* heterometallic assemblies based on orbitally degenerate heptacyanidorhenate(IV) were prepared and structurally characterized. An analysis of the magnetic data of polycrystalline samples showed that both compounds display slow magnetization relaxation at temperatures below 5 K. The very low temperature measurements of the magnetization on the single crystals demonstrate that for the *1D* compound $\{[Mn(SB^{2+})Re(CN)_7]\cdot 7H_2O\}_n$ (**1**) and the *0D* complex $[Mn(SB^{2+})(H_2O)Re(CN)_7]\cdot 2H_2O$ (**2**), the hysteresis loops open just below 2.2 and 1.8 K, respectively. Thus, heterometallic polymer **1** is the first single-chain magnet involving a pentagonal bipyramidal $[Re^{IV}(CN)_7]^{3-}$ synthon, and the binuclear complex **2** represents a single-molecule magnet.

Keywords: cyanide-bridged heterometallic assemblies; heptacyanidorhenate(IV); Mn(III) Schiff base complexes; single-molecule magnet; single-chain magnet; *1D* coordination polymers; slow magnetic relaxation

Citation: Sukhikh, T.S.; Wolfgang, W.; Vostrikova, K.E. Slow Magnetic Relaxation in Neutral *0D* and *1D* Assemblies of a Mn(III) Schiff Base Complex and Heptacyanorhenate(IV). *Magnetochemistry* **2022**, *8*, 126. https://doi.org/10.3390/magnetochemistry8100126

Academic Editor: Xiaoqing Zhao

Received: 26 September 2022
Accepted: 11 October 2022
Published: 14 October 2022

1. Introduction

Orbitally degenerate *4d*/*5d* cyanidometallates with unquenched orbital angular momentum are efficient sources of strong magnetic anisotropy in the design of molecular nanomagnets, which were first predicted theoretically [1,2] and then confirmed experimentally by synthesis of a number of single-molecule magnets (SMMs) based on these homoleptic complexes as highly anisotropic building blocks [3–10]. An important feature of these complexes is the absence of single-ion magnetic anisotropy due to their low-spin ground state ($S = 1/2$). In this case, magnetic anisotropy is produced cooperatively, in concert with attached high-spin 3d ions, through anisotropic exchange interactions, underlying an alternative strategy toward high-performance SMMs [1,2]. In contrast to rather numerous cyanide-bridged *1D* magnetic systems involving 3*d* metal ions [11–16], the single-chain magnets (SCMs) incorporating homoleptic cyanide complexes of heavier *d* metal ions are considerably less common [17–22]. Among these, the unidimensional magnetic polymers based on low-spin ($S = 1/2$) orbitally degenerate cyanidometallates are particularly rare, with only a few SCMs based on hexacyanides of iron(III) [23–26] and osmium(III) [17], and four *1D* coordination polymers involving heptacyanidomolibdate(III) [27,28], only three of which are SCMs.

The low-spin octahedral nd^5 complexes $[M^{III}(CN)_6]^{3-}$, M^{III} = Fe, Ru, Os [6,24,29], as well as the pentagonal bipyramidal complexes $[Mo^{III}(CN)_7]^{4-}$ ($4d^3$) [30] and $[Re^{IV}(CN)_7]^{3-}$ ($5d^3$) [3,31], display anisotropic exchange interactions with linked high-spin 3*d* ions. An energy barrier U, which has to be surmounted to reverse the magnetization, determines the slow relaxation of magnetization in the low-dimensional (*LD*) assemblies comprising these tectons. The *U* value for an SMM depends on the uniaxial anisotropy energy of a molecule. For a *1D* polymer, the appearance of slow magnetic relaxation was predicted by Glauber [32]. Unlike SMMs, the energy barrier in SCMs depends not only on the magnetic anisotropy strength but also on the magnitude of intrachain magnetic coupling [16]. Hence,

it should be easier to increase the *U* value for SCMs than for SMMs. As previously stated, a neutral *1D* polymer based on the low-spin hexacyanoferrate(III) and Mn^{III} Schiff base (SB) complex can display SCM behavior [23]. This alternating [-Mn^{III}-NC-Fe^{III}-CN-] system comprises two sources of magnetic anisotropy: zero-field splitting (ZFS) of the $[Mn^{III}SB]^{3+}$ unit with an easy magnetization axis along the Jahn–Teller distortion direction, and angular orbital momentum L of the $[Fe(CN)_6]^{3-}$ unit. Due to the relatively small spin–orbit coupling (SOC) of the latter (ζ_{Fe} = 464 cm^{-1} [33]) *L* may be quite quenched depending on the degree of distortion from the perfect octahedral (O_h) geometry. This was confirmed by our comparative study [24] of two anionic SCMs with a general formula $(X)_2[Mn^{III}(acacen)Fe^{III}(CN)_6]$ (X = Et_4N^+ or Ph_4P^+; acacen = N,N′-ethylenebis(acetylacetonylideneaminato) and the same magnetic core fragment (–Fe–CN–Mn–NC). These chains display (since these are inherent properties of substances, therefore it always exists, and not only when we studied theme) noticeably different blocking temperatures (T_b) of ~1.1 and 2.5 K, respectively. To prevent the *L* quenching and provide stronger exchange interactions (since the heavier metal ions possess more diffuse *4(5)d*-orbitals), we used the complex $[Os(CN)_6]^{3-}$ as a metalloligand with $5d^5$ electronic configuration and higher SOC [34,35]. As a result, the only SCM (this is not only the first SCM, but so far the only one) composed of hexacyanidoosmate(III) was prepared and studied [17].

Inspired by the above achievements, we aimed to obtain a similar anionic chain comprising another orbitally degenerate heptacyanidorhenate(IV) magnetic unit (Scheme 1a) not only possessing sufficiently strong spin–orbit splitting (ζ_{Re} = 2400 cm^{-1}) [35], but also possessing a coordination polyhedron with a pronounced uniaxial symmetry. However, our attempts to prepare an SCM starting from $[Mn(acacen)]^+$ and $[Re(CN)_7]^{3-}$ resulted in highly anisotropic *3D* [31] and *2D* [19] networks. In addition, the efforts to prepare the anionic chains based on the triply charged octacyanidometallates of Mo^V and W^V, were unsuccessful because the cationic complex $[Mn(acacen)]^+$ (Scheme 1b) formed layered systems with the $[M^V(CN)_8]^{3-}$ in the presence of Ph_4P^+ [36] or PPN^+ (bis(triphenylphosphine)iminium) [37].

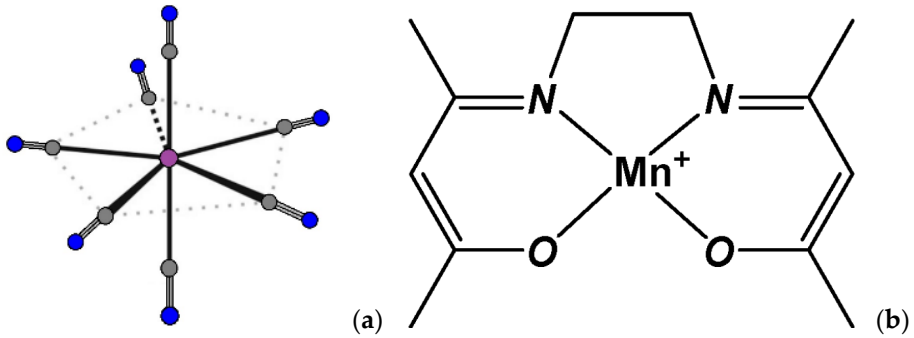

Scheme 1. Building units: (**a**) pentagonal bipyramidal $[Re(CN)_7]^{3-}$ (D_{5h} symmetry); (**b**) $[Mn(acacen)]^+$.

The present study is a continuation of our previous research directed toward the design of *LD* bimetallic nanomagnets involving orbitally degenerate cyanidometallates and Mn^{III} Schiff base complexes. Here, we present the synthesis, crystal structure description, and preliminary magnetic studies of two neutral assemblies incorporating a *salen*-type complex $[Mn^{III}(SB^{2+})]^{3+}$ (Scheme 2): the first SCM based on pentagonal bipyramidal Re^{IV} heptacyanide (Scheme 1a), $\{[Mn(SB^{2+})Re(CN)_7]\cdot 7H_2O\}_n$ (**1**), and a binuclear compound, $[Mn(SB^{2+})(H_2O)Re(CN)_7]\cdot 2H_2O$ (**2**). The crystals of the latter were obtained as a result of a prolonged recrystallization process of the chain polymer.

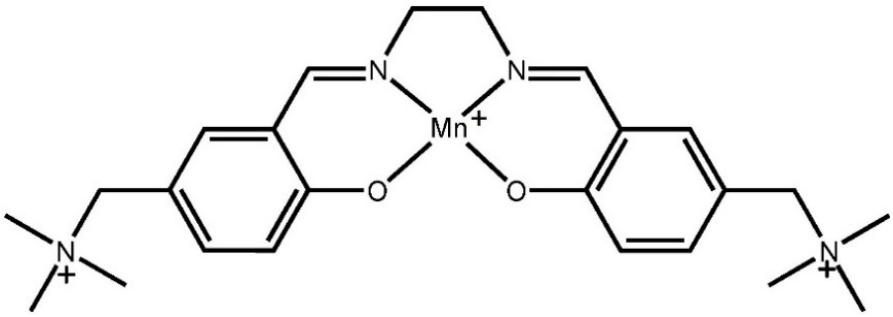

Scheme 2. Molecular structure of triply charged *salen*-type $[Mn(SB^{2+})]^{3+}$.

2. Results and Discussion

2.1. Synthetic Approach

Electroneutrality is a fundamental force in the self-assembly of heterometallic coordination compounds in solution. The Mn^{III} complexes with Schiff bases of both the *salen* and *acacen* type ordinarily have a charge of +1; therefore, when they interact with triply charged anions of cyanidometallates, three times as many of them (3:1 ratio) are required to ensure the electroneutrality of the system. This combination does not guarantee the formation of *LD* heterometallic assemblies with the axial symmetry of a heterometallic system. However, at a ratio of 1:2, for the diamagnetic dianion $[Fe(CN)_5NO]^{2-}$ and $[Mn^{III}(acacen)]^{+}$, the neutral *0D* and *1D* polynuclear compounds were obtained along with a layered material $\{[(Mn^{III}(acacen))_2Fe(CN)_5NO]\}_n$ [38] depending on the solvent used.

Previously, we successfully obtained the first neutral heterobimetallic cyanide-bridged compounds involving one anisotropic Mn^{III} complex and one octacyanidotungstate(V) per molecular unit. One of them—$[Mn(SB^{2+})(H_2O)W^{V}(CN)_8]\cdot 5H_2O$, obtained via slow diffusion of component solutions—is a discrete molecule, while the other—$\{[Mn(SB^{2+})(H_2O)W^{V}(CN)_8]\cdot 8H_2O\}_n$, precipitated during a rapid mixing of the reagents—is a *1D* polymer exhibiting SCM properties [18]. Therefore, in order to obtain the neutral low-dimensional species incorporating $[Re^{IV}(CN)_7]^{3-}$, we used the same manganese(III) complex $[Mn(SB^{2+})(H_2O)_2](ClO_4)_3\cdot H_2O$. However, in the case of heptacyanidometallate(IV), the process of self-assembly of bimetallic compounds occurs somewhat differently. When layering an acetonitrile solution of $(Bu_4N)_3[Re(CN)_7]$ on an aqueous solution of a manganese(III) complex, the large dark crystals of a chain polymer (**1**) are formed on the walls of the test tube, and then crumble in air due to the partial loss of solvate water molecules. Compound **1** can also be obtained in the form of a finely crystalline powder by dropping a solution of an Mn^{III} complex into a solution of cyanidometallate: $[Mn(SB^{2+})(H_2O)_2](ClO_4)_3 + (Bu_4N)_3[Re(CN)_7] + H_2O \rightarrow \{[Mn(SB^{2+})Re(CN)_7]\cdot 7H_2O\}_n\downarrow + 3Bu_4NClO_4$ (for more details, see the Section 4). The slow recrystallization of powdered compound **1** in aqueous media resulted in formation of crystals of **2**—the binuclear compound $[Mn(SB^{2+})(H_2O)Re(CN)_7]\cdot 2H_2O$—in a small amount: $\mathbf{1}_{powder} + H_2O \rightarrow \mathbf{2}_{crystals}$. According to X-ray powder diffraction data, the initial powder of the chain polymer was only partially transformed into a dimer species (see below).

2.2. Crystal Structure Description

The crystallographic data and structural refinement summary for **1** and **2** are included in Table S1 (see Supplementary Materials). Single crystal X-ray structural analysis revealed that compound **2** has a *0D* molecular structure, while **1** is a *1D* chain polymer. The molecular views of the repeating unit in the chain $\{[Mn(SB^{2+})Re(CN)_7]\}_n$ (**1**) and an asymmetric unit of $[Mn(SB^{2+})(H_2O)Re(CN)_7]\cdot 2H_2O$ (**2**) are shown in Figure 1. Both compounds are neutral bimetallic assemblies consisting of one $[Re(CN)_7]^{3-}$ anion and one cation ($[Mn(SB^{2+})]^{3+}$ for **1** or $[Mn(SB^{2+})(H_2O)]^{3+}$ for **2**).

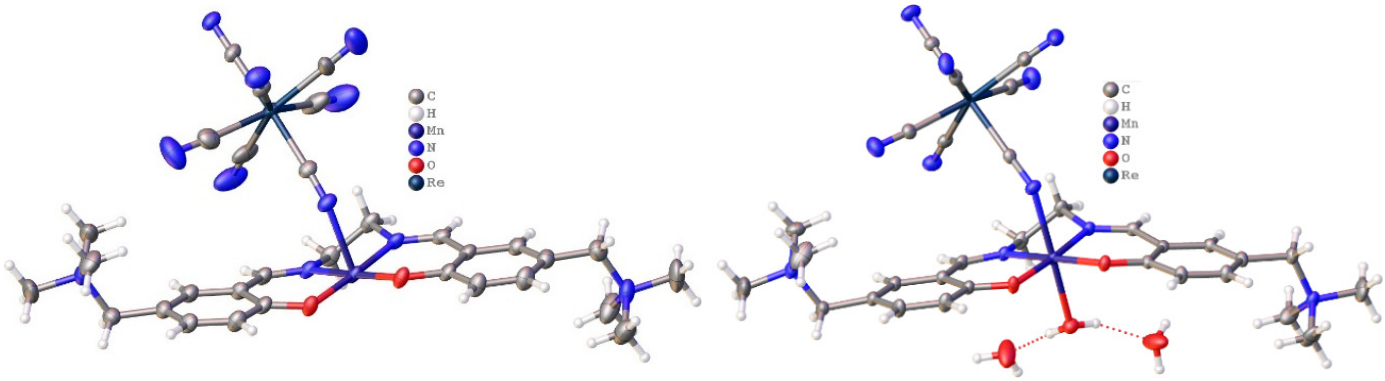

(**a**) (**b**)

Figure 1. Molecular structure of (**a**) the repeating unit in the chain $\{[Mn(SB^{2+})Re(CN)_7]\}_n$ (**1**) (solvent water molecules are omitted) and (**b**) the molecular unit $[Mn(SB^{2+})(H_2O)Re(CN)_7](H_2O)_2$ in **2**. ORTEP diagrams are made with 50% probability thermal ellipsoids.

In both compounds, a slightly distorted pentagonal bipyramidal coordination environment of the Re center comprises seven cyanide ligands. In fact, $[Re(CN)_7]^{3-}$ is much less distorted than its isoelectronic counterpart, $[Mo(CN)_7]^{4-}$ [8,20,28]. The Re−C distances are in the range 2.061(5)–2.144(5) Å, with an average of 2.106(19) Å, similar to that observed for $(Bu_4N)_3[Re(CN)_7]$ (2.064(10)–2.123(11) Å) [39]. The coordination environment of the Mn ion is an elongated tetragonal bipyramid because of the Jahn–Teller distortion. The 2O and 2N donor atoms of the SB^{2+} ligand in the basal plane of the pyramid form shorter bonds of 1.877–1.989 Å, while the axial bonds are much longer, i.e., 2.242–2.299 Å.

The $Mn–(N{\equiv}C)_{axial}$ bond angle departs considerably from 180° and is equal to 144.2° and 145.1° for **1** and **2**, respectively, being close to a value of 144.4° for $\{[Mn(SB^{2+})Fe(CN)_6]\}_n$ [23]. It should be noted that such a flexion is typical of the cyanide-bridged $Mn^{III}–M(CN)_n$ complexes [9,34,38,40–42]. However, for the complexes of SB^{2+}, which is a sterically demanding ligand, this angle is especially small. For example, for a much less bulky SB complex $[Mn(acacen)]^+$, the value of this angle for the Re^{IV}-Mn^{III} system varies in the range 152.9–163.7° [31,36,37]. At the same time, the Mn–(N≡C) angle is 162.6 and 160.1° in the discrete species $[Mn(^{Me}SB^{2+})(H_2O)Fe(CN)_6]$ [9] and $[Mn(SB^{2+})(H_2O)W(CN)_8]$ (**3**) [18], respectively.

In contrast to the heterobimetallic $\{Mn^{III}(SB)M(CN)_m\}$ complexes—where SB is a *salen*-type ligand, for which a dimerization of the $Mn^{III}(SB)$ fragments is quite widespread (see, for example, [25,43])—the trications $[Mn(SB^{2+})H_2O]^{3+}$ in the *0D* neutral moieties based on hexa- and heptacyanidometallates are not dimerized in a crystal due to the *trans* location of the $[Me_3N^+CH_2]$ substituents relative to the SB^{2+} plane (Figure 1 and Figure S1). Meanwhile, the binuclear molecules of **3** [18] are dimerized due to hydrogen bounding, π–π stacking of the ligand aromatic rings, and non-valent CN ... H interactions of the $[Me_3N^+CH_2]$ groups. As a result, the latter are in *cis* positions relative to one another.

As in the case of the neutral *1D* polymer involving hexacyanidometallates [23], in its congener **1**, the Jahn–Teller axes (JTA) of the $[Mn^{III}(SB^{2+})]^{3+}$ moieties are ideally aligned along the chain direction without a bending angle (Figure 2 and Figure S2), while the apical axes of the rhenium cyanide (AAR) are close to perpendicular at 104.1°, the latter being slightly flatter than the 97.9° observed in $\{[Mn(SB^{2+})Fe(CN)_7]{\cdot}4H_2O\}_n$ [23]. A similar situation is observed for the packing of the *0D* binuclear compound **2** (Figure S3), with JTA and AAR angles of 172.7° and of 67.7°, respectively.

Visually, the small crystals of the binuclear compound **2** are more resistant to the loss of solvate water molecules compared with the large crystals of the chain compound **1**, whose crystals crumble within a few days, depending on the temperature and humidity of the surrounding air. The elemental analysis data additionally testify in favor of the latter. This difference is due to the features of the packing and strength of hydrogen bonds in the crystals of **1** and **2**. In the latter, a system of hydrogen bonds links the discrete

binuclear molecules in the chains (Figure 3) bounded in the layers (Figure S4), which are interconnected by the sufficiently short contacts C≡N . . . H-C and C-O . . . HC of ~2.5 Å. The chain packing in a crystal of compound **1** leads to the formation of channels enclosing the majority of the solvate H_2O molecules (Figure S5).

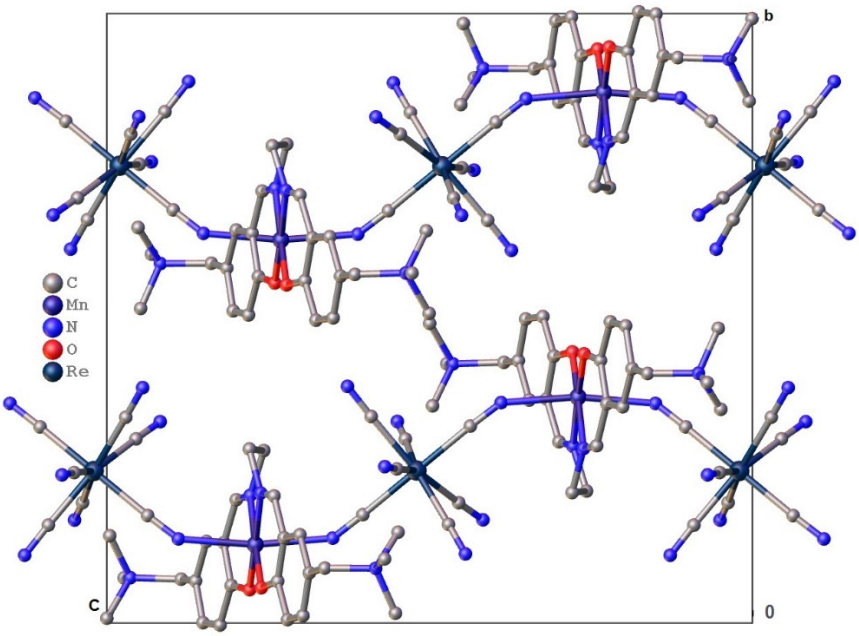

Figure 2. View of the chain motifs projected along the *a*-axis. Hydrogen atoms and interstitial water molecules have been omitted for clarity.

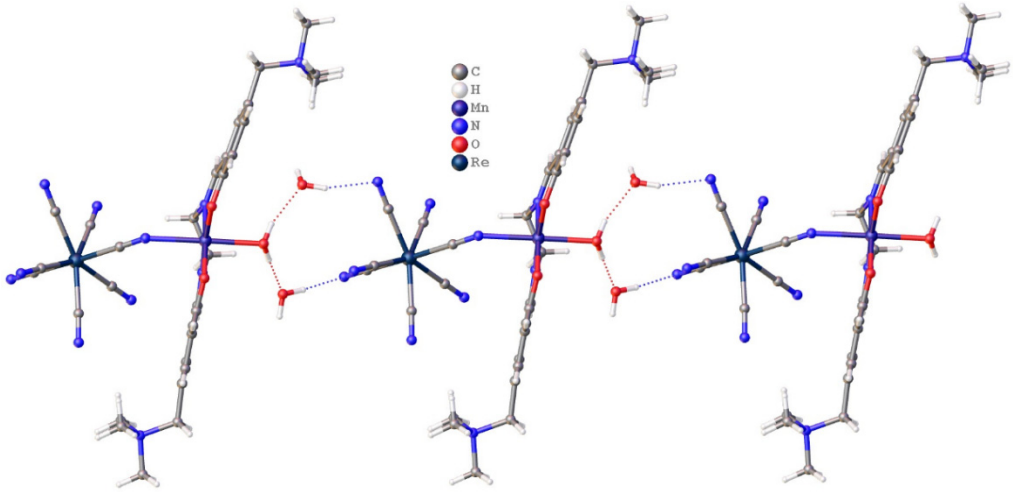

Figure 3. The *1D* motif formation in **2**. A view along the *b*-axis.

2.3. Characterization of the Polycrystalline Samples

Since **1** and **2** have sufficiently similar chemical composition, which varies depending on partial loss of solvate water, the main methods for their identification are IR spectroscopy and X-ray phase analysis. Significant differences can be observed in the IR spectra of the compounds not only in the region of C≡N stretching vibrations, but also in the area associated with ligand vibrations (Figure 4). More spectroscopic information is presented in Figures S6–S8 in the SI.

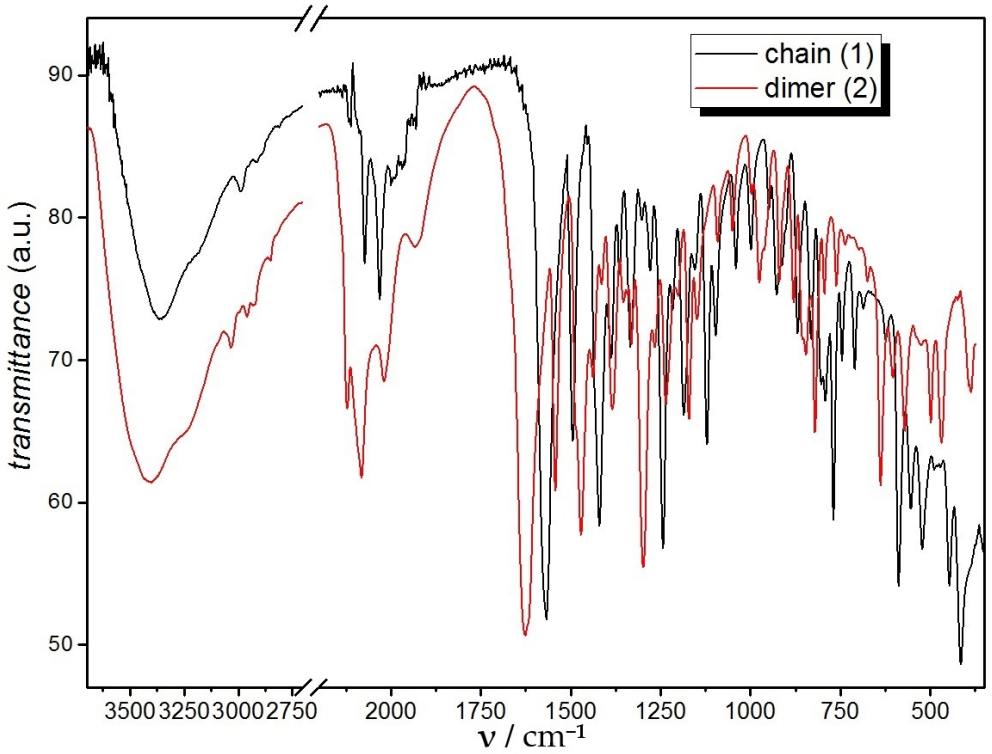

Figure 4. IR spectra for **1** and **2**, registered for the single-crystal batches.

According to the IR and PXRD data (Figure S9), bimetallic complex **1** prepared by a precipitation technique (see the Section 4) is identical to the crystals obtained by a slow diffusion technique. As mentioned above, a small amount (singular) of crystals of **2** was obtained via prolonged recrystallization of the powdered compound **1** in water. According to the PXRD study (Figure S10), the original powder present in the reaction vessel was not completely converted from a chain into a dimer even after six months.

2.4. Investigation of Magnetic Properties

2.4.1. Static Magnetic Behavior

The temperature dependence of the *dc* molar susceptibility for the powder sample of **1**, measured in an applied field of 1000 Oe, is shown in Figure 5 as a χT versus T plot. At 300 K, the observed χT value of 3.68 is close to the 3.60 emu K mol^{-1} expected for one Mn^{III} (S = 2, g = 2.03) [31] and one Re^{IV} (S = 1/2, g = 2.33) [39] as magnetically uncoupled spin carriers. Starting from room temperature, χT first decreases slightly and then reaches a shallow minimum of 3.28 emu K mol^{-1} at ~75 K. This behavior of χT is characteristic of antiferromagnetic interactions between the Mn^{III} and Re^{IV} centers within the chains [31,44]. Below 50 K, χT increases and reaches a sharp maximum of 9.30 emu·K·mol^{-1} at ~5 K, before dropping to 6.48 emu K mol^{-1} at 2 K.

The non-compensation of the spins induces a ferrimagnetic arrangement along the chain, giving rise to a repeating unit with S = 3/2. As the temperature drops below 5 K, χT decreases sharply, owing to the field saturation of the magnetization and the magnetic anisotropy of the Re^{IV} centers.

The magnetization vs. field curve of **1** measured at 2 K reveals complete reversibility of the magnetization (inset of the Figure 5). The M value reached at 50 kOe is equal to 2.86 μ_B per Mn^{III}–Re^{IV} unit, which is far from 5 μ_B (the theoretical value corresponding to the five unpaired electrons). The estimated saturation magnetic field (H_A) for **1** using the experimental data M(H) is about 151 kOe, which is significantly greater than the values of 100, 108, and 120 kOe found for SCMs based on neutral $[(SB^{2+})(Cr/Fe)(CN)_6]$ units [23] and anionic $[Mn^{III}(acacen)Fe^{III}(CN)_6]^{2-}$ [17] fragments, respectively.

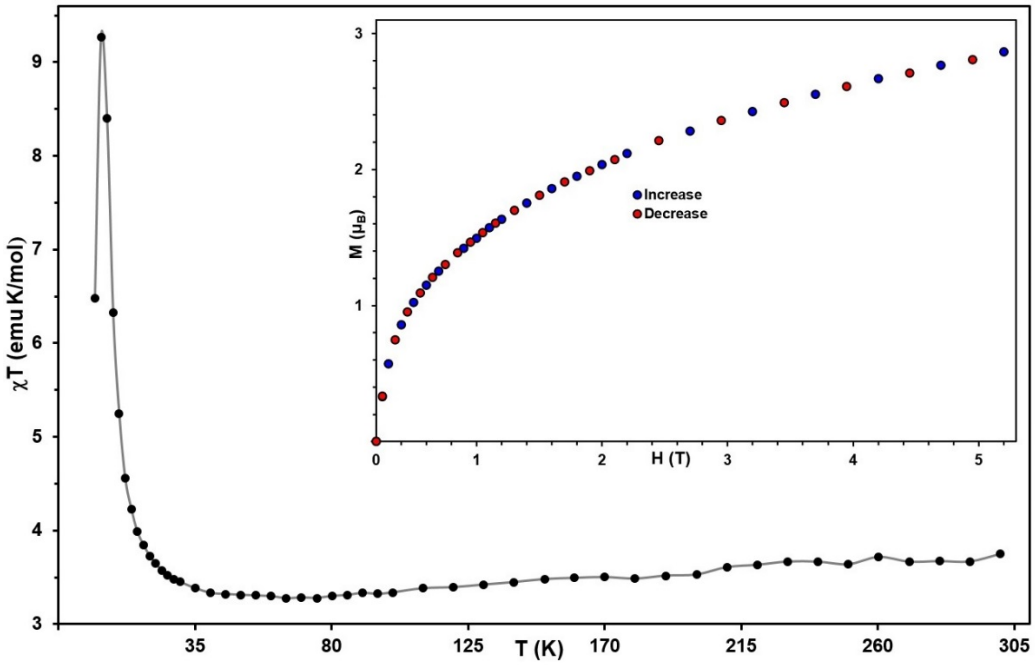

Figure 5. Magnetic *dc* plots for **1**. Temperature dependence of χT at H = 1000 Oe (solid line guides the eyes). Inset: magnetization versus the field at T = 2 K.

The magnetic behavior of **2** was studied on a sample consisting of the crystals manually sorted from the possible powder impurities of the *1D* precursor. At first glance, the magnetic behavior of **2** (Figure 6) was very similar to that of **1**; the temperature dependence of χT also had a sharp maximum, and the shape of the plots for M(H) was also similar. However, the devil is in the details.

The χT value of 3.68 emu·K·mol^{-1} at 300 K precisely coincides with that registered for **2**. Furthermore, unlike **1**, χT increases slowly, pointing to a ferromagnetic interaction between the spins, with about 3.85 emu·K·mol^{-1} at 70 K, after which the χT values begin to rise, reaching a peak of 8.21 emu·K·mol^{-1} at 5 K before dropping sharply at lower temperatures. The presence of the pronounced peak on the χT plot at a temperature of about 5 K is quite unexpected for a *0D* compound, since no such a peak is found in the temperature dependence of the related dimers $[Et_4N]_2[Mn(saldmen)(H_2O)Fe(CN)_6]\cdot MeOH\cdot 4H_2O$ (**3**) [45] and $[Mn^{III}(^{Me}SB^{2+})(H_2O)Fe(CN)_6]\cdot 7H_2O\cdot MeCN$ (**4**) ($^{Me}SB^{2+}$ = (*R*)-*N*,*N*′-(1-methylethylene) bis(5-trimethylammoniomethylsalicylideneiminate. For the latter, the χT value remains practically constant up to sufficiently low temperatures, and then drops sharply at T < 15 K. On lowering the temperature, the χT of **3** gradually increases from 3.45 emu·K·mol^{-1}, reaching a flat maximum of 3.91 emu·K·mol^{-1} at 26 K, and then decreases to ~3.25 (3.88) emu·K·mol^{-1}. The authors believe that this decrease is due to the ZFS of the Mn^{III} ion and/or an intermolecular antiferromagnetic interaction. However, when dimer **3** is desolvated, its magnetic behavior changes significantly. Lowering the temperature results in a gradual decrease in χT, which shows a round minimum at ca. 60 K. It then increases abruptly to reach a value of 18.6 emu·K·mol^{-1} at 1.9 K (at H_{dc} = 600 Oe), which is much higher than that of the largest possible spin state $S_T = 5/2$, where χT = 4.38 emu·K·mol^{-1}. This behavior of **3′** is reminiscent of that shown by **1**, with the difference that, for the latter, at low temperatures, the saturation of χT occurs at H = 1000 Oe instead of 600 Oe for **3′**, the molar susceptibility of **3′** is not saturated at 1.9 K, and H_{DC} = 1 Oe.

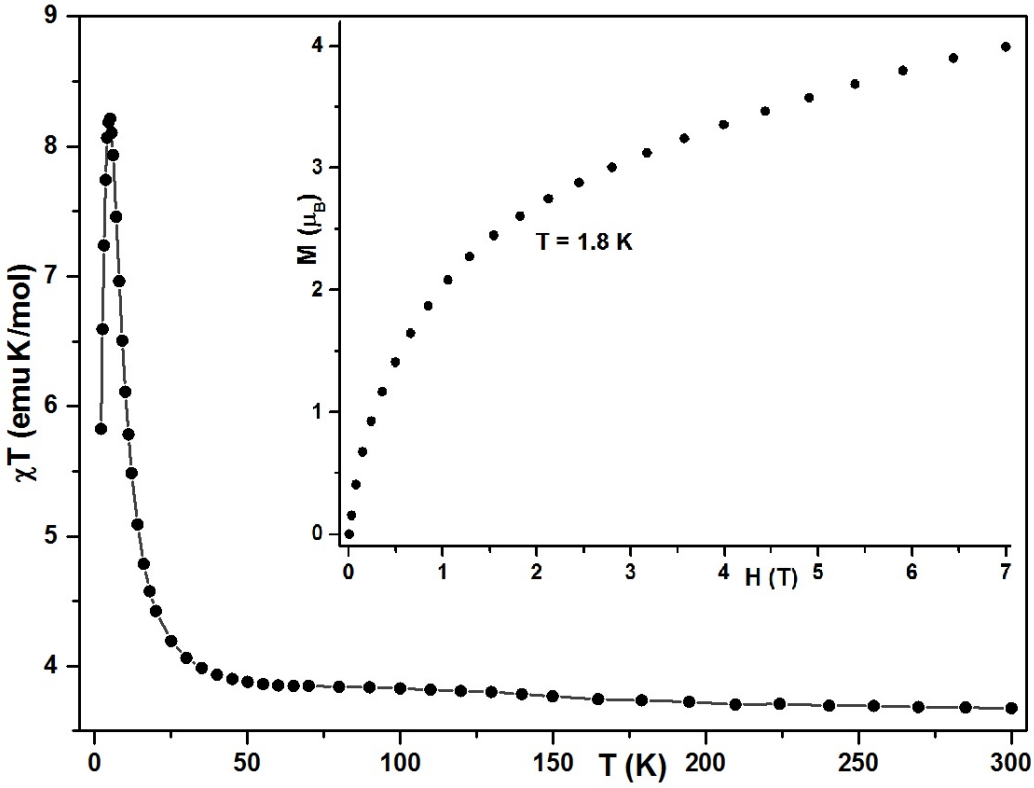

Figure 6. Magnetic dc plots for **2**. Temperature dependence of χT at H = 1000 Oe (solid line). Inset: magnetization versus the field at T = 2 K.

The variable-field plot of the magnetization for **2** is presented in Figure 6. It should be noted that the value of M of 3.58 μ_B at 50 kOe is close to the 3.45 μ_B shown by **3** and exceeds the value for **1** by 0.72 μ_B. For **2**, the M value at the maximum available field of 70 kOe is 3.99 μ_B—the estimated for ferromagnetically coupled Mn^{III} ($S = 2$) and Re^{IV} ($S = \frac{1}{2}$) with a $g_{av} = 2.0$ magnetic field H_A being about 120 kOe. This is less than the estimated lower limit of the saturation magnetic field, H_A, for **2**.

Unlike the chain, the *0D* compound displays magnetic hysteresis at T = 1.8 K (Figure S11), with a very small coercive field of 156 Oe.

2.4.2. AC Magnetic Measurements

Although the χT plots of compounds **1** and **2** are similar at temperatures lower than 30 K, the dependences of the two compounds differ. The temperature-variable behavior of the *ac* molar susceptibilities of **1** measured in the frequency range of 1–1200 Hz in an oscillating ac magnetic field of 2.7 Oe and a zero *dc* field are presented in Figure S12 (SI). These data clearly indicate that both the real and imaginary parts of the susceptibility have a pronounced frequency dependence below 4 K.

Unfortunately, the lower temperature limit available for commercial SQUID magnetometers (down to ~2 K) is not sufficient to reliably determine the full set of relaxation parameters for the *1D* compound, since the magnetization-blocking temperature T_b for **1** appears to be below 2 K. This conclusion follows from the fact that not a single curve from the set of plots of the imaginary part of the magnetic susceptibility χ''(T), at various frequencies, reaches a maximum. Below, we present a few SCM parameters estimated for **1** from the experimental data.

The correlation length, ξ, of a *1D* classical polymer is directly proportional to the χT product in a zero applied field. In the particular cases of the Ising-like or anisotropic Heisenberg models, ξ and, thus, χT increase exponentially with decreasing temperature as follows: $\chi T \approx C_{eff} \times \exp(\Delta_\xi / k_B T)$, where C_{eff} is the effective Curie constant and Δ_ξ is the energy required to create a domain wall along the chain [12,46]. Therefore, to determine the

SCM behavior of a material, the $\ln(\chi'T)$ versus $1/T$ plot (χ' being the real *ac* susceptibility data collected in $H^{dc} = 0$ at the lowest available *ac* frequency) must be thoroughly examined. Its linear dependence, with a slope corresponding to Δ_{ξ}, proves the *1D* magnetic nature of the material and the presence of significant magnetic anisotropy. Figure S14 (SI) shows the respective $\ln(\chi'T)$ versus $1/T$ plots for **1**. A linear region is observed in the temperature range 10–6 K, giving $C_{eff} = 1.005$ emu K mol^{-1} and $\Delta\xi/k_B = 6.66$ K. At 4.5 K, $\ln(\chi'T)$ reaches a maximum ($(\chi'T)_{max} = 10.3$ emu K mol^{-1}) and then experiences a linear decrease with decreasing temperature until χ' is blocked under an oscillation of 1 Hz. An intersection of the two linear regions, occurring at ca. 4.5 K, corresponds to the crossover temperature (T^*), where the magnetic correlation becomes physically limited by crystalline defects, and temperatures below T^* comprise the finite-sized regime [47].

The dynamic magnetic behavior of the heterobinuclear compound **2** was studied for a polycrystalline sample in the frequency range of 1–1500 Hz under an oscillating *ac* magnetic field of 3.5 Oe. The dependences of the *ac* molar susceptibility at the *dc* fields of 0 and 200 Oe are practically the same for **2**, as shown by the variable-field test carried out at 2 K (Figure S13). Therefore, a study of the temperature dependences of the *ac* molar susceptibility for **2** at different frequencies was performed at $H_{dc} = 100$ Oe (see Figure S15). Both sets of plots indicate the presence of two relaxation processes. This may be due either to a manifestation of two different relaxation mechanisms, or to the presence of a second magnetic phase. In our opinion, the latter option is the most plausible explanation, since a stratum of a desolvated solid could be formed on the surface of the compound **2** crystals.

Despite the fact that the binuclear molecules in compound **2** are connected in layers by a network of hydrogen bonds, such intermolecular coupling can appear only at very low temperatures, because they are too low in energy compared to the covalent bonds of bridging cyanides. Therefore, down to temperatures of ~10 K, the deviations from the high-temperature value of χT can only be caused by the M(CN)–Mn(SB) exchange interaction, as is observed for **1**. At very low temperatures, the positive or negative "bend" of the χT plot is usually determined by the intermolecular interaction, whether ferro- (as in the case of **3′**) or antiferromagnetic in nature. Examples of the latter include the complexes $[M^{II}L_2(ROH)_2]$ (M^{II} = Ni, Co; R = H, Me, Et; L is a CF_3-decorated enamine ketone derivative of stable 3-imidazoline nitroxide) [48–51], in which the bis-chelate metal complexes are woven into a 2D network through hydrogen bonds between the ROH and nitroxyl groups of adjacent molecules: M-^{R}OH . . . $^{\cdot}$O–N–(M). A removal of coordinated ROH molecules also leads to an essential change in the magnetic behavior due to the formation of covalent metal–radical bonds, leading to the formation of a 1D compound [52].

As can be seen in Figure 3, the dimer fragments of **2** are connected in a chain due to a set of hydrogen bonds: (Mn–OH_2) . . . (solvate H_2O) . . . (N≡C–Re). The removal of at least one solvate water molecule necessarily leads to the reorganization of the entire packing of binuclear fragments and, as a result, the modification of the intermolecular contacts and geometric parameters inside the dimer. With the complete removal of water from **2**, the formation of a *1D* polymer is possible, in which $[Mn(SB^{2+})]^{3+}$ complexes are connected to Re^{IV} ions by an apical and equatorial cyanide bridge (see Figure S16). Such an organization of the chain should promote mutual alignment of both the apical axes of the heptacyanidorhenate anions and the Jahn–Teller axes of the $[Mn(SB^{2+})]^{3+}$ cations in the crystal, which is important to increase the coercivity of low-dimensional magnets. It should be noted that the determined by the Mn–(N≡C) angle mutual slope of the $(N{\equiv}C–Re–C{\equiv}N)_{apical}$ and N–Mn–N axes is responsible for the nature and magnitude of the intrachain exchange interaction affecting the spin reversal barrier height and the value of T_b.

2.4.3. Magnetic Measurements at Very Low Temperatures

By means of an in-house-made μ-SQUID system, additional *M* versus *H* data down to 30 mK (Figure 7 and Figure S17) were collected from single crystals. As shown in Figure 7 for **1**, the M/M_s (M_s is a saturation field) versus *H* hysteresis loop opens below 1.6 K, and the temperature lower than 2 K was used to study the polycrystalline sample of **2**. The

coercivity of 1.3 T is observed for a crystal of **1** at 0.4 K. This value is somewhat less than the 1.68 T obtained for the Fe congener $\{[Mn(SB^{2+})Fe(CN)_7]\cdot 4H_2O\}_n$ [23]. Considering the *1D* nature of **1**, as demonstrated by the analysis of correlation length discussed above ($\ln(\chi' T)$ versus $1/T$ plot; Figure S14), the slow relaxation of magnetization evident from the *M* versus *H* hysteresis loops strongly supports the view that **1**, with $T_b \approx 1.6$ K, is a new example of a single-chain magnet.

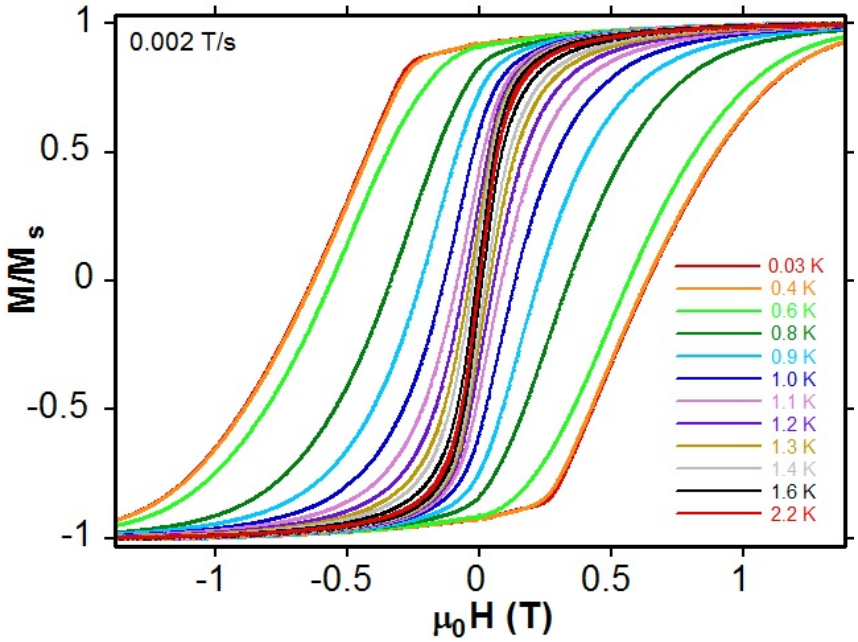

Figure 7. Field dependences of the normalized magnetizations at 0.002 T s^{-1} measured at low temperatures from oriented single crystals of **1** with the H^{dc} applied along the easy magnetic axis.

Despite the presence of magnetic hysteresis, the pronounced frequency dependence of the molar magnetic susceptibility, and the *0D* structure, the classification of the relaxation nature (SMM or SCM) of compound **2** is not clear, for several reasons. In contrast to **1**, a magnetic hysteresis loop for **2** is already visible at 1.8 K on a polycrystalline sample (Figure S11). Moreover, as shown by low-temperature studies (Figure S18a), the shape of the hysteresis and the coercivity of **2** are preserved for a single crystal up to 0.8 K. At 0.5 K, the coercivity at H = 0 collapses and, starting from ~0.4 K, the shape of the hysteresis changes. This behavior may also be associated with the presence of the aforementioned dehydrated layer, which leads to the coexistence of two different magnetic phases with two different magnetization-blocking temperatures of ~1.8 and ~0.4 K—presumably for *1D* and *0D* species, respectively. This hypothesis is also supported by the presence of linear segments on the ln(X′T) vs. $1/T$ plot (Figure S14b).

3. Conclusions and Perspectives

The two neutral low-dimensional heterobimetallic compounds based on the binuclear magnetic unit $[Mn^{III}(SB^{2+})Re(CN)_7]$ were obtained and structurally characterized. Preliminary studies of their magnetic behavior showed that compound **1**, $\{[Mn(SB^{2+})Re(CN)_7](H_2O)_7\}_n$, is the first SCM involving orbitally degenerate pentagonal bipyramidal heptacyanidorhenate, and its blocking temperature is T_b ~1.6 K. The nature of the χT behavior in the high-temperature range for *1D* and *0D* differs significantly, confirming the ferrimagnetic and ferromagnetic character of magnetic exchange interactions (EIs) for the first and the second, respectively. However, at temperatures below 60 K, ferromagnetic EIs prevail in both compounds up to a temperature of 4.5 K, where a maximum is observed in the χT-*T* plot, and then χT rapidly decreases due to saturation in the field effect. For both compounds, even under a field of 70 kOe, the magnetization does not reach the maximum value of 5 μ_B expected for

five unpaired electrons. This is due to the high anisotropy of these systems, as evidenced by the estimated values of the fields H_A of 151 and 120 kOe for **1** and **2**, respectively.

The results of static and dynamic magnetic measurements for **2** show that the studied sample likely contains two phases, since its small crystals were apparently dehydrated in the near-surface layer at the time of measurement. Analysis of the crystal packing of compound **2** shows that its structure is formed by hydrogen bonds' *1D* motifs, which, upon dehydration, could turn into covalently bonded chains that are structurally different from those of **1**.

The unusual magnetic properties of both compounds originate from the interplay of Re–Mn anisotropic spin coupling and the ZFS effect of Mn^{III} ions with a noncollinear orientation of the local magnetic axes in crystals of the compounds.

Unfortunately, the magnetization-blocking temperatures were low and were just outside the range of commercial SQUID magnetometers, so we were unable to obtain a dataset sufficient to obtain a complete set of quantitative parameters for magnetic relaxation of **1** and **2** by simulating the experimental data. We need to obtain low-temperature data for the decays with time of the normalized magnetizations measured from oriented single crystals to be able to estimate the barriers $\Delta_{\tau 1}$ and $\Delta_{\tau 2}$ for the two compounds [23]. In addition, we are planning studies aimed at obtaining compound **2** in a different way than the time-consuming recrystallization of **1**, in order to ensure reproducible synthesis of the binuclear compound in quantities sufficient for detailed characterization (including TG, DSC, and PXRD methods) of the solvated phase of **2**, as well as its dehydrated derivative. This will make it possible to conduct a complete study of the static and relaxation magnetic properties of each form separately. The obtained experimental data will be used for theoretical modeling in order to determine the magnetic characteristics for anisotropic exchange, as was done using microscopic theory for *3D* $[(Mn^{III}acacen)_3Re^{IV}(CN)_7]_n$ [31] and $[\{MnL^{N5}(H_2O)\}_2Mo(CN)_7]$ [30]. In the longer term, we plan to produce doubly connected SCMs such as $\{[M(bida)(H_2O)]_2[Mo(CN)_7]\cdot 6H_2O\}_n$ [20].

4. Materials and Methods

All of the reagents and solvents (EKOS-1, Moscow, Russia) were used without further purification; $[Mn(SB^{2+})(H_2O)_2](ClO_4)_3\cdot H_2O$ [41] and $(Bu_4N)_3[Re(CN)_7]$ [39] were prepared using published protocols.

The polycrystalline powder material of $\{[Mn(SB^{2+})Re(CN)_7]\cdot 7H_2O\}_n$ (**1**) was obtained via a precipitation method using a 1:3 mixture of water and acetonitrile as the solvent.

A dark-brown solution of $[Mn(SB^{2+})(H_2O)_2](ClO_4)_3\cdot 2H_2O$ (41 mg, 0.05 mmol) in 2.5 mL of solvent was added dropwise to a stirred light-yellow solution of $(Bu_4N)_3[Re(CN)_7$ (55 mg, 0.05 mmol) in 2.5 mL of solvent. The reaction mixture was stirred while heating until boiling. The precipitated dark product was centrifuged and then washed twice with H_2O (2 mL), twice with MeCN (2 mL), once with Et_2O (2 mL), and then air-dried. The yield was 95%. $C_{31}H_{34}MnN_{11}O_2Re\cdot 4.5(H_2O)$ (914.89); CHN: calcd. C 40.70, H 4.74, N 16.84; found C 40.8, H 4.5, N 16.95. IR (ATR) $\bar{\upsilon}_{(CN)}$: 2111.8(sh), 2073.1, 2030.6, 1999.8(sh), 1969.0(sh) 1930.4 (sh) cm^{-1}.

The crystals of **1** were obtained via slow diffusion of reagent solutions. First, 2 mL of an aqueous solution containing 41 mg of manganese complex was placed in a glass test tube (0.8 cm × 10 cm), on which a buffer layer was placed (1:1 mixture of H_2O:MeCN, 1.5 mL). The top layer was a solution of rhenium cyanide (55 mg in 2 mL of MeCN). The tubes were closed with parafilm and stored in the dark at a temperature of +4 °C. Three weeks later, rather large dark-brown crystals and a polycrystalline powder were obtained. The crystals were manually separated from the powder (~9 mg) and used for X-ray diffraction studies and magnetic measurements.

The crystals of $[Mn(SB^{2+})(H_2O)Re(CN)_7]\cdot 2H_2O$ (**2**): The powder of **1** was placed in a test tube covered with several mL of distilled water. The test tube closed with parafilm was kept in a dark place at room temperature. A few months later, the water was partially evaporated, and small dark parallelepiped-like crystals formed on the walls of the test tube near the upper frontier

of the liquid. IR (ATR) $\bar{\upsilon}_{(CN)}$: 2121.7(sh), 2081.2, 2019.5, 1932.7(sh), $C_{31}H_{34}MnN_{11}O_2Re{\cdot}3H_2O$ (887.87); CHN: calcd. C 41.94, H 4.54, N 17.35; found C 42.1, H 4.4, N 17.4.

Elemental (C,H,N) analysis were carried out with a Euro-Vector 3000 analyzer (Eurovector, Redavalle, Italy). FTIR spectra were measured with a NICOLET spectrophotometer (Thermo Electron Scientific Instruments LLC, Madison, WI, USA) in the 4000–375 cm^{-1} range. Powder X-ray measurements were performed using Cu-Kα radiation (λ = 1.5418 Å) with an X'Pro powder diffractometer (PANalytical Inc., Almelo, The Netherlands) at room temperature. All magnetic measurements of properties were performed using a Quantum Design MPMS 5XL SQUID magnetometer (Quantum Design, Inc., San Diego, CA, USA) in the temperature range of 1.8–300 K and under a magnetic field of up to 50 kOe. The magnetic susceptibility χ_m is the molar magnetic susceptibility per mole of $C_{31}H_{34}MnN_{11}O_2Re{\cdot}7H_2O$ and $C_{31}H_{34}MnN_{11}O_2Re{\cdot}3H_2O$ units, and was corrected for the diamagnetic contribution calculated from Pascal's constants [53]. Ultralow-temperature (>1.8 K) magnetization measurements on single crystals were performed using a μ-SQUID array [54].

Single-crystal XRD experimental details are presented in Table S1 (Supplementary Materials). Crystallographic data were deposited with the Cambridge Crystallographic Data Centre (deposit numbers CCDC 1569081-1569082). Copies of the data can be obtained free of charge via https://www.ccdc.cam.ac.uk/structures/ (accessed on 10 August 2022) (or from the Cambridge Crystallographic Data Centre, 12, Union Road, Cambridge, CB2 1EZ, UK; Fax: +44 1223 336033; e-mail: deposit@ccdc.cam.ac.uk).

Supplementary Materials: The following supporting information can be downloaded at: https://www.mdpi.com/article/10.3390/magnetochemistry8100126/s1, Figure S1: A view of chains' packing in a crystal of 1 demonstrating a translocation of the $[Me_3N^+CH_2]$ substituents relative to the SB^{2+} plane. Hydrogen atoms are omitted for clarity; Table S1: SCXRD experimental details; Figure S2: A layer formation in a crystal of 1: H_2O molecules bind the fragments $[Mn^{III}(SB^{2+})]^{3+}$ and $[Re(CN)_7]^{3-}$ belonging to the different chains. The layers are interconnected by means of interstitial water molecules. The SB^{2+} ligands are reduced for clarity; Figure S3: A view of dimers' packing in a crystal of 2. The SB^{2+} ligands are reduced, and hydrogen atoms are omitted for clarity; Figure S4: A layer formation in a crystal of 2: H_2O molecules bind the fragments $[Mn^{III}(SB^{2+})]^{3+}$ and $[Re(CN)_7]^{3-}$ belonging to the different chains. The layers are interconnected by means of interstitial water molecules. The hydrogen atoms are partially omitted for clarity; Figure S5: A view (in the c-axis direction) of channels in a crystal of 1: (a) filled by water molecules, (b) empty; Figure S6: IR spectrum for $\{[Mn(SB^{2+})Re(CN)_7]{\cdot}7H_2O\}_n$ 1; Figure S7: IR spectrum for the precursor $[Mn(SB^{2+})(H_2O)_2](ClO_4)_3{\cdot}H_2O$; Figure S8: IR spectrum for the precursor $(Bu_4N)_3[Re(CN)_7]{\cdot}H_2O$ (KBr); Figure S9: PXRD patterns for the chain compound 1: polycrystalline sample (black), theoretically calculated (red); Figure S10: PXRD patterns for the dimer compound 2 (room temperature) and theoretical calculations (150 K) for 1 and 2; Figure S11: Magnetic hysteresis loop of 2 measured at 1.8 K on a polycrystalline sample (sw. rate—0.07 $T{\cdot}s^{-1}$); Figure S12: Variable temperature of the real, χ' (top), and imaginary, χ'' (bottom), parts of the *ac* molar susceptibility data for 1 under H_{dc} = 0 Oe, H_{ac} = 2.7 Oe. Solid lines are guides; Figure S13: Frequency dependence of the real (χ') (top), and imaginary (χ'') (bottom), parts of the *ac* susceptibility for a polycrystalline sample of 2 in different *dc*-fields y and with applied a 3 Oe *ac* field. Solid lines are guides; Figure S14: Plots of $\ln(X'T)$ vs. $1/T$ (where X′ is the molar component of the *ac* susceptibility) for 1 (top) and 2 (bottom) collected in a zero applied *dc* field and at a frequency of 1 Hz. The dashed red lines correspond to a linear fit for the high-temperature region, giving Δ_ξ/k_B = 6.66 (C_{eff} = 1.005 emu·K/mol) and 4.21 K (C_{eff} = 1.526 emu·K/mol) for 1 and 2, respectively. The dashed green lines correspond to a linear fit for the low-temperature region. An intersection of the two linear regions corresponds to the crossover temperature $T^* \approx 4.5$ K, which is equal for both; Figure S15: Variable-temperature real, χ' (top), and imaginary, χ'' (bottom), *ac* molar susceptibility data for 2 under H_{dc} = 100 Oe, H_{ac} = 3.5 Oe. Solid lines are guides; Figure S16: Possible formation of a *1D* polymer from 2 by desolvation. The $[Mn(SB^{2+})]^{3+}$ complexes are connected to the Re^{IV} ions by equatorial and apical cyanide bridges; Figure S17: Field dependences of the normalized magnetization at the field-sweeping rates of 0.002 $T{\cdot}s^{-1}$ (a), and 0.140 $T{\cdot}s^{-1}$ (b), measured at different temperatures on an oriented single crystal of 2 with the magnetic field applied along the easy magnetic axis; Figure S18: Field dependences of the normalized magnetization at 0.03 K (a), and 0.2 K (b) measured at different field sweeping rates on an oriented single

crystal of 2 with the magnetic field applied along the easy magnetic axis. The maximum coercitivity reaches1043.5 Oe at 30 mK and SwRate of 0.280 $T \cdot s^{-1}$.

Author Contributions: Conceptualization, K.E.V.; funding acquisition, K.E.V.; investigation, K.E.V., W.W., and T.S.S.; supervision K.E.V.; visualization, K.E.V.; writing—original draft, K.E.V.; writing—review and editing, K.E.V. and W.W. All authors have read and agreed to the published version of the manuscript.

Funding: This research was funded by the Ministry of Science and Higher Education of the Russian Federation (No. 121031700313-8 and No. 121031700321-3).

Institutional Review Board Statement: Not applicable.

Informed Consent Statement: Not applicable.

Data Availability Statement: Not applicable.

Acknowledgments: The authors are grateful to Marko Damjanovic for magnetic data collection.

Conflicts of Interest: The authors declare no conflict of interest.

References

1. Mironov, V.S.; Chibotaru, L.F.; Ceulemans, A. Mechanism of a Strongly Anisotropic $Mo^{III}-CN-Mn^{II}$ Spin−Spin Coupling in Molecular Magnets Based on the $[Mo(CN)_7]^{4-}$ Heptacyanometalate: A New Strategy for Single-Molecule Magnets with High Blocking Temperatures. *J. Am. Chem. Soc.* **2003**, *125*, 9750–9760. [CrossRef] [PubMed]
2. Mironov, V.S. New Approaches to the Problem of High-Temperature Single-Molecule Magnets. *Dokl. Phys. Chem.* **2006**, *408*, 130–136. [CrossRef]
3. Freedman, D.E.; Jenkins, D.M.; Iavarone, A.T.; Long, J.R. A Redox-Switchable Single-Molecule Magnet Incorporating $[Re(CN)_7]^{3-}$. *J. Am. Chem. Soc.* **2008**, *130*, 2884–2885. [CrossRef] [PubMed]
4. Zadrozny, J.M.; Freedman, D.E.; Jenkins, D.M.; Harris, T.D.; Iavarone, A.T.; Mathonière, C.; Clérac, R.; Long, J.R. Slow Magnetic Relaxation and Charge-Transfer in Cyano-Bridged Coordination Clusters Incorporating $[Re(CN)_7]^{3-/4-}$. *Inorg. Chem.* **2010**, *49*, 8886–8896. [CrossRef] [PubMed]
5. Wang, X.-Y.; Avendaño, C.; Dunbar, K.R. Molecular Magnetic Materials Based on 4d and 5d Transition Metals. *Chem. Soc. Rev.* **2011**, *40*, 3213. [CrossRef] [PubMed]
6. Dreiser, J.; Pedersen, K.S.; Schnegg, A.; Holldack, K.; Nehrkorn, J.; Sigrist, M.; Tregenna-Piggott, P.; Mutka, H.; Weihe, H.; Mironov, V.S.; et al. Three-Axis Anisotropic Exchange Coupling in the Single-Molecule Magnets $NEt_4[Mn^{III}{}_2(5\text{-}Brsalen)_2(MeOH)_2M^{III}(CN)_6]$ (M=Ru, Os). *Chem. Eur. J.* **2013**, *19*, 3693–3701. [CrossRef]
7. Qian, K.; Huang, X.-C.; Zhou, C.; You, X.-Z.; Wang, X.-Y.; Dunbar, K.R. A Single-Molecule Magnet Based on Heptacyanomolybdate with the Highest Energy Barrier for a Cyanide Compound. *J. Am. Chem. Soc.* **2013**, *135*, 13302–13305. [CrossRef] [PubMed]
8. Wu, D.-Q.; Shao, D.; Wei, X.-Q.; Shen, F.-X.; Shi, L.; Kempe, D.; Zhang, Y.-Z.; Dunbar, K.R.; Wang, X.-Y. Reversible On–Off Switching of a Single-Molecule Magnet via a Crystal-to-Crystal Chemical Transformation. *J. Am. Chem. Soc.* **2017**, *139*, 11714–11717. [CrossRef]
9. Ishikawa, R.; Nakano, M.; Breedlove, B.K.; Yamashita, M. Syntheses, Structures, and Magnetic Properties of Discrete Cyano-Bridged Heterodinuclear Complexes Composed of MnIII(Salen)-Type Complex and $M_{III}(CN)_6$ Anion (M_{III} = Fe, Mn, and Cr). *Polyhedron* **2013**, *64*, 346–351. [CrossRef]
10. Shi, L.; Wei, X.; Wang, X.; Wu, D. Research Progress in Molecular Magnetic Materials Based on the $[Mo(CN)_7]^{4-}$ Unit. *Sci. Sin. Chim.* **2020**, *50*, 1637–1653. [CrossRef]
11. Miyasaka, H.; Saitoh, A.; Abe, S. Magnetic Assemblies Based on Mn(III) Salen Analogues. *Coord. Chem. Rev.* **2007**, *251*, 2622–2664. [CrossRef]
12. Coulon, C.; Miyasaka, H.; Clérac, R. Single-Chain Magnets:Theoretical Approach and Experimental Systems BT. In *Single-Molecule Magnets and Related Phenomena*; Winpenny, R., Ed.; Springer: Berlin/Heidelberg, Germany, 2006; pp. 163–206. ISBN 978-3-540-33240-4.
13. Sun, H.-L.; Wang, Z.-M.; Gao, S. Strategies towards Single-Chain Magnets. *Coord. Chem. Rev.* **2010**, *254*, 1081–1100. [CrossRef]
14. Dhers, S.; Feltham, H.L.C.; Brooker, S. A Toolbox of Building Blocks, Linkers and Crystallisation Methods Used to Generate Single-Chain Magnets. *Coord. Chem. Rev.* **2015**, *296*, 24–44. [CrossRef]
15. Bar, A.K.; Pichon, C.; Sutter, J.-P. Magnetic Anisotropy in Two- to Eight-Coordinated Transition–Metal Complexes: Recent Developments in Molecular Magnetism. *Coord. Chem. Rev.* **2016**, *308*, 346–380. [CrossRef]
16. Coulon, C.; Pianet, V.; Urdampilleta, M.; Clérac, R. Single-Chain Magnets and Related Systems BT. In *Molecular Nanomagnets and Related Phenomena*; Gao, S., Ed.; Springer: Berlin/Heidelberg, Germany, 2014; pp. 143–184. ISBN 978-3-662-45723-8.
17. Peresypkina, E.V.; Majcher, A.M.; Rams, M.; Vostrikova, K.E. A Single Chain Magnet Involving Hexacyanoosmate. *Chem. Commun.* **2014**, *50*, 7150–7153. [CrossRef]

18. Majcher, A.M.; Pilet, G.; Mironov, V.S.; Vostrikova, K.E. Neutral Low-Dimensional Assemblies of a Mn(III) Schiff Base Complex and Octacyanotungstate(V): Synthesis, Characterization, and Magnetic Properties. *Magnetochemistry* **2017**, *3*, 16. [CrossRef]
19. Vostrikova, K.E. Low-Dimensional Heterometallic Assemblies Involving Orbitally Degenerate Cyanometallate and Displaying Slow Magnetic Dynamics. *J. Magn. Magn. Mater.* **2018**, *459*, 71–77. [CrossRef]
20. Shi, L.; Shao, D.; Wei, X.; Dunbar, K.R.; Wang, X. Enhanced Single-Chain Magnet Behavior via Anisotropic Exchange in a Cyano-Bridged Mo^{III}–Mn^{II} Chain. *Angew. Chem. Int. Ed.* **2020**, *59*, 10379–10384. [CrossRef]
21. Charytanowicz, T.; Jankowski, R.; Zychowicz, M.; Chorazy, S.; Sieklucka, B. The Rationalized Pathway from Field-Induced Slow Magnetic Relaxation in Co^{II}–W^{IV} Chains to Single-Chain Magnetism in Isotopological CoII–WV Analogues. *Inorg. Chem. Front.* **2022**, *9*, 1152–1170. [CrossRef]
22. Tan, P.; Yang, Y.; Lv, W.; Jing, R.; Cui, H.; Zheng, S.-J.; Chen, L.; Yuan, A.; Chen, X.-T.; Zhao, Y. A Cyanometallate- and Carbonate-Bridged Dysprosium Chain Complex with a Pentadentate Macrocyclic Ligand: Synthesis, Structure, and Magnetism. *New J. Chem.* **2022**, *46*, 7892–7898. [CrossRef]
23. Miyasaka, H.; Madanbashi, T.; Saitoh, A.; Motokawa, N.; Ishikawa, R.; Yamashita, M.; Bahr, S.; Wernsdorfer, W.; Clérac, R. Cyano-Bridged Mn^{III}-M^{III} Single-Chain Magnets with M^{III}=Co^{III}, Fe^{III}, Mn^{III}, and Cr^{III}. *Chem. Eur. J.* **2012**, *18*, 3942–3954. [CrossRef] [PubMed]
24. Rams, M.; Peresypkina, E.V.; Mironov, V.S.; Wernsdorfer, W.; Vostrikova, K.E. Magnetic Relaxation of 1D Coordination Polymers X_2[Mn(acacen)Fe$(CN)_6$], X = Ph_4P^+, Et_4N^+. *Inorg. Chem.* **2014**, *53*, 10291–10300. [CrossRef] [PubMed]
25. Ferbinteanu, M.; Miyasaka, H.; Wernsdorfer, W.; Nakata, K.; Sugiura, K.; Yamashita, M.; Coulon, C.; Clérac, R. Single-Chain Magnet $(NEt^4)[Mn^2(5\text{-}MeOsalen)^2Fe(CN)^6]$ Made of $Mn^{III}-Fe^{III}-Mn^{III}$ Trinuclear Single-Molecule Magnet with an $S = 9/2$ Spin Ground State. *J. Am. Chem. Soc.* **2005**, *127*, 3090–3099. [CrossRef]
26. Aguilà, D.; Jeannin, O.; Fourmigué, M.; Jeon, I.-R. Mn^{III}–Fe^{III} Heterometallic Compounds within Hydrogen-Bonded Supramolecular Networks Promoted by an $[Fe(CN)^5(CNH)]^{2-}$ Building Block: Structural and Magnetic Properties. *Inorg. Chem.* **2018**, *57*, 7892–7903. [CrossRef]
27. Wei, X.-Q.; Qian, K.; Wei, H.-Y.; Wang, X.-Y. A One-Dimensional Magnet Based on $[Mo^{III}(CN)_7]^{4-}$. *Inorg. Chem.* **2016**, *55*, 5107–5109. [CrossRef]
28. Wang, K.; Xia, B.; Wang, Q.-L.; Ma, Y.; Liao, D.-Z.; Tang, J. Slow Magnetic Relaxation Based on the Anisotropic Ising-Type Magnetic Coupling between the MoIII and MnII Centers. *Dalton Trans.* **2017**, *46*, 1042–1046. [CrossRef] [PubMed]
29. Pinkowicz, D.; Southerland, H.I.; Avendaño, C.; Prosvirin, A.; Sanders, C.; Wernsdorfer, W.; Pedersen, K.S.; Dreiser, J.; Clérac, R.; Nehrkorn, J.; et al. Cyanide Single-Molecule Magnets Exhibiting Solvent Dependent Reversible "On" and "Off" Exchange Bias Behavior. *J. Am. Chem. Soc.* **2015**, *137*, 14406–14422. [CrossRef]
30. Mironov, V.S. Origin of Dissimilar Single-Molecule Magnet Behavior of Three Mn II 2 Mo III Complexes Based on [Mo III (CN) 7] 4– Heptacyanomolybdate: Interplay of Mo III –CN–Mn II Anisotropic Exchange Interactions. *Inorg. Chem.* **2015**, *54*, 11339–11355. [CrossRef] [PubMed]
31. Samsonenko, D.G.; Paulsen, C.; Lhotel, E.; Mironov, V.S.; Vostrikova, K.E. $[Mn_{III}(SchiffBase)]_3[Re_{IV}(CN)_7]$, Highly Anisotropic 3D Coordination Framework: Synthesis, Crystal Structure, Magnetic Investigations, and Theoretical Analysis. *Inorg. Chem.* **2014**, *53*, 10217–10231. [CrossRef]
32. Glauber, R.J. Time-Dependent Statistics of the Ising Model. *J. Math. Phys.* **1963**, *4*, 294–307. [CrossRef]
33. Graham, M.J.; Zadrozny, J.M.; Shiddiq, M.; Anderson, J.S.; Fataftah, M.S.; Hill, S.; Freedman, D.E. Influence of Electronic Spin and Spin–Orbit Coupling on Decoherence in Mononuclear Transition Metal Complexes. *J. Am. Chem. Soc.* **2014**, *136*, 7623–7626. [CrossRef]
34. Vostrikova, K.E. Homoleptic Osmium Cyanide Complexes: Synthesis and Perspective Application in Molecular Magnetism. In *Osmium: Synthesis Characterization and Applications*; Wise, G., Ed.; Nova Science Publishers: New York, NY, USA, 2015; pp. 43–78. ISBN 978-1-63483-517-6.
35. David, J.; Mendizábal, F.; Arratia-Pérez, R. Electronic Structure and Molecular Properties of the Heptacyanorhenate $[Re(CN)^7]^{3-}$ and $[Re(CN)^7]^{4-}$ Complexes. *J. Phys. Chem. A* **2006**, *110*, 1072–1077. [CrossRef]
36. Sukhikh, T.S.; Vostrikova, K.E. *1567014: Experimental Crystal Structure Determination*; Cambridge Crystallographic Data Centre: Cambridge, UK, 2017. [CrossRef]
37. Sukhikh, T.S.; Vostrikova, K.E. *1567013: Experimental Crystal Structure Determination*; Cambridge Crystallographic Data Centre: Cambridge, UK, 2017. [CrossRef]
38. Peresypkina, E.V.; Vostrikova, K.E. 2[Mn(Acacen)]$^+$ + $[Fe(CN)_5NO]^{2-}$ Polynuclear Heterobimetallic Coordination Compounds of Different Dimensionality in the Solid State. *Dalton Trans.* **2012**, *41*, 4100. [CrossRef]
39. Bennett, M.V.; Long, J.R.R. New Cyanometalate Building Units: Synthesis and Characterization of $[Re(CN)^7]^{3-}$ and $[Re(CN)_8]^{3-}$. *J. Am. Chem. Soc.* **2003**, *125*, 2394–2395. [CrossRef]
40. Lescouëzec, R.; Toma, L.M.; Vaissermann, J.; Verdaguer, M.; Delgado, F.S.; Ruiz-Pérez, C.; Lloret, F.; Julve, M. Design of Single Chain Magnets through Cyanide-Bearing Six-Coordinate Complexes. *Coord. Chem. Rev.* **2005**, *249*, 2691–2729. [CrossRef]
41. Sakamoto, F.; Sumiya, T.; Fujita, M.; Tada, T.; Tan, X.S.; Suzuki, E.; Okura, I.; Fujii, Y. T-Site Selective Photocleavage of DNA by Cationic Schiff Base Complex of Manganese(III). *Chem. Lett.* **1998**, *27*, 1127–1128. [CrossRef]
42. Pinkowicz, D.; Podgajny, R.; Nowicka, B.; Chorazy, S.; Reczyński, M.; Sieklucka, B. Magnetic Clusters Based on Octacyanidometallates. *Inorg. Chem. Front.* **2015**, *2*, 10–27. [CrossRef]

43. Sukhikh, T.; Vostrikova, K. Assembly of Mn(III) Schiff Base Complexes with Heptacyanorhenate(IV). *Inorganics* **2017**, *5*, 59. [CrossRef]
44. Harris, T.D.; Bennett, M.V.; Clérac, R.; Long, J.R. $[ReCl_4(CN)_2]^{2-}$: A High Magnetic Anisotropy Building Unit Giving Rise to the Single-Chain Magnets $(DMF)_4MReCl_4(CN)_2$ (M = Mn, Fe, Co, Ni). *J. Am. Chem. Soc.* **2010**, *132*, 3980–3988. [CrossRef]
45. Miyasaka, H.; Ieda, H.; Re, N.; Crescenzi, R.; Floriani, C. Assembling Bi-, Tri- and Pentanuclear Complexes into Extended Structures Using a Desolvation Reaction: Synthesis, Structure, and Magnetic Properties of Manganese(III)−Schiff-Base−Hexacyanoferrate Polymeric Compounds and Their Derived Extended Structures. *Inorg. Chem.* **1998**, *37*, 255–263. [CrossRef]
46. Nakamura, K.; Sasada, T. Statistical Mechanics of Classical One-Dimensional Heisenberg Ferromagnets with Single-Site Anisotropy. *J. Phys. C Solid State Phys.* **1978**, *11*, 331–343. [CrossRef]
47. Miyasaka, H.; Julve, M.; Yamashita, M.; Clérac, R. Slow Dynamics of the Magnetization in One-Dimensional Coordination Polymers: Single-Chain Magnets. *Inorg. Chem.* **2009**, *48*, 3420–3437. [CrossRef] [PubMed]
48. Ovcharenko, V.I.; Vostrikova, K.E.; Ikorskii, V.N.; Larionov, S.V.; Sagdeev, R.Z. The Low Temperature Ferromagnet dimethanol-bis-[2,2,5,5-tetramethyl-1-oxyl-3-imidazoline-4-(3′,3′,3′-trifluoromethyl-1′-propenyl-2′-oxyato)] Cobalt(II), $CoL_2(CH_3OH)_2$. *Dokl. Akad. Nauk SSSR* **1989**, *306*, 660–662.
49. Ovcharenko, V.I.; Vostrikova, K.E.; Romanenko, G.V.; Ikorski, V.N.; Podberezskaya, N.V.; Larionov, S.V. Synthesis, Crystal Structure and Magnetic Properties of Di(Methanol) and Di(ethanol)-bis-2,2,5,5-tetramethyl-1-oxyl-3-imidazoline-4-(3′,3′,3′-trifluoromethyl-1-propenyl-2′-oxyato Nickel(II)—A New Type of Low Temperature Ferromagnetics. *Dokl. Akad. Nauk SSSR* **1989**, *306*, 115–118.
50. Vostrikova, K.E.; Ovcharenko, V.I.; Romanenko, G.V.; Ikorskii, V.N.; Podberezskaya, N.V.; Reznikov, V.A.; Volodarskii, L.B. Synthesis, Structure and Magnetic-Properties of Bis-chelate Complexes of Zinc(II), Copper(II), Cobalt(II) and Nickel(II) with Derivatives of 3-Imidazoline Nitroxyl Radical. *Russ. J. Inorg. Chem.* **1992**, *37*, 1755–1772.
51. Ovcharenko, V.I.; Vostrikova, K.E.; Podoplelov, A.V.; Sagdeev, R.Z.; Romanenko, G.V.; Ikorskii, V.N. The Synthesis and Magnetic Properties of Two Different Water-Containing Layered Polymeric Ni^{II} Complexes with a 3-Imidazoline Nitroxide. The Low Efficiency of Exchange Interactions through the OH-bridges of Water Molecules. *Polyhedron* **1994**, *13*, 2781–2792. [CrossRef]
52. Ovcharenko, V.I.; Romanenko, G.V.; Ikorskii, V.N.; Musin, R.N.; Sagdeev, R.Z. Polymorphous Modifications of a Ni^{2+} Complex with Stable Nitroxide Involving Ni^{2+}–O–N Bonds. Quantum-Chemical Investigation of Exchange Interactions in Heterospin Systems. *Inorg. Chem.* **1994**, *33*, 3370–3381. [CrossRef]
53. Bain, G.A.; Berry, J.F. Diamagnetic Corrections and Pascal's Constants. *J. Chem. Educ.* **2008**, *85*, 532. [CrossRef]
54. Wernsdorfer, W. Classical and Quantum Magnetization Reversal Studied in Nanometer-Sized Particles and Clusters. In *Advances in Chemical Physics*; John and Wiley and Sons: Hoboken, NJ, USA, 2001; pp. 99–190. ISBN 9780470141786.